

Assessing the validity of the anelastic and Boussinesq approximations to model solar inertial modes

Suprabha Mukhopadhyay¹, Yuto Bekki¹, Xiaojue Zhu¹, and Laurent Gizon^{1,2}

¹ Max-Planck-Institut für Sonnensystemforschung, Justus-von-Liebig-Weg 3, 37077 Göttingen, Germany

² Institut für Astrophysik und Geophysik, Georg-August-Universität Göttingen, Friedrich-Hund-Platz 1, 37077 Göttingen, Germany
e-mail: gizon@mps.mpg.de e-mail: zhux@mps.mpg.de

Received / accepted

ABSTRACT

Context. Global-scale inertial modes of oscillations have been recently observed on the Sun. They might play an important dynamic and diagnostic role for the Sun.

Aims. This work aims to assess the validity of simplifying assumptions in the equation of continuity, which have often been used in the linear models of solar inertial modes.

Methods. We compute the linear eigenmodes of the Sun's convection zone in the inertial frequency range using the Dedalus code. This single framework enables us to compare the sensitivity of the modes to different model setups, such as the compressible setup and the Boussinesq and anelastic approximations. We consider both the cases of uniform rotation and solar differential rotation (as given by helioseismology).

Results. We find that the compressible and anelastic models have almost identical eigenmodes, under uniform rotation and solar differential rotation. On the other hand, the absence of density stratification in the Boussinesq model results in significantly different eigenmodes under these setups. The differences are most prominent for the non-toroidal modes with significant radial motions mainly due to the absence of the compressional β -effect.

Conclusions. The anelastic approximation simplifies the calculations and reduces the numerical cost without affecting the solar inertial modes. The Boussinesq or incompressible approximations cannot be used to model the solar inertial modes accurately. Since the effects of differential rotation on the eigenmodes are very significant, an acceptable setup is to use the anelastic approximation together with the solar differential rotation.

Key words. Sun: oscillations - Sun: interior - Sun: rotation - Hydrodynamics - Instabilities

1. Introduction

The Sun undergoes various oscillations through which we can probe deep into its interior. The p modes are acoustic modes of oscillation restored by pressure and have a timescale of minutes (e.g., [Christensen-Dalsgaard 2002](#)). They have successfully been used to infer the Sun's large-scale flows, internal differential rotation (e.g., [Schou et al. 1998](#); [Larson & Schou 2018](#)) and meridional circulation (e.g., [Giles et al. 1997](#); [Gizon et al. 2020a](#)). Modes in the inertial frequency range – ‘inertial modes’ for short – are low-frequency modes of oscillation restored by the Coriolis force (e.g., [Greenspan 1969](#)). Their periods are in order of the Sun's rotation period.

1.1. Solar observations

All observed inertial modes were first detected in the horizontal flow field on the Sun's surface. They are most easily described as waves of radial vorticity that propagate retrograde in a frame that co-rotates with the Sun's Carrington rotation rate (approximately the equatorial rotation rate). By convention, in this paper, we always use the Carrington rotation rate as a reference when using the terms retrograde and prograde. The observed inertial modes belong to several classes (see [Gizon et al. 2024](#), for a review). The equatorial Rossby modes follow the well-known classical dispersion relation for the sectoral Rossby modes of

uniformly rotating fluid for azimuthal wavenumbers in the range $3 \leq m \leq 30$ ([Löptien et al. 2018](#); [Liang et al. 2019](#); [Proxauf et al. 2020](#); [Hanson & Hanasoge 2024](#)). Their retrograde propagation is due to the planetary β -effect, i.e., the latitudinal variation of the tangential component of the Coriolis force ([Vallis 2006](#)). [Gizon et al. \(2021\)](#) found many additional quasi-toroidal global inertial modes of oscillation in the solar data. Among these modes are high-latitude modes with $m = 1, 2, 3$. These global modes can have either symmetric or antisymmetric north-south vorticity. Their velocity eigenfunctions display a characteristic spiral pattern in the polar regions. The mode with the largest velocity amplitude (~ 15 m/s) is the $m = 1$ high-latitude mode with north-south symmetric radial vorticity; it is present in daily-cadence solar Dopplergrams over the last five solar cycles ([Liang & Gizon 2024](#)). We note that the velocity pattern associated with this $m = 1$ mode had been reported before but misidentified as giant convection cells ([Hathaway et al. 2013](#)). In addition to high-latitude modes, many other modes, with m up to at least 10, have been observed with amplitudes that peak at mid-latitudes, near their critical latitudes. The critical latitude of a mode is the latitude where its phase speed equals the local rotation velocity. Modes that are retrograde (with respect to the equatorial rotation rate) can have critical latitudes since the Sun's rotation rate decreases with latitude (with the sharpest decrease above 60°). All the modes described above, including the equatorial Rossby and high-latitude modes, have critical latitudes.

Table 1. Classes of solar inertial modes studied in this paper.

mode names used here	other names	observed on the Sun?	propagation direction in Carrington frame	north-south symmetry of radial vorticity	linear models
$n = 0$ equatorial Rossby	...	yes (1–4)	retrograde	symmetric	(1), (7–11)
high-latitude inertial	...	yes (5)	retrograde	both symmetries	(5), (9)
HFR	mixed modes	yes (6)	retrograde	anti-symmetric	(11–13)
$n = 1$ equatorial Rossby	mixed modes	maybe (4)	retrograde	symmetric	(9), (11–12)
prograde columnar	thermal Rossby; Busse columns	not yet	prograde	anti-symmetric	(9), (14–18)

References. (1) Löptien et al. (2018); (2) Liang et al. (2018); (3) Proxauf et al. (2020); (4) Hanson & Hanasoge (2024); (5) Gizon et al. (2021); (6) Hanson et al. (2022); (7) Gizon et al. (2020b); (8) Fournier et al. (2022); (9) Bekki et al. (2022b); (10) Triana et al. (2022); (11) Bhattacharya & Hanasoge (2023); (12) Jain et al. (2024); (13) Bekki (2024); (14) Roberts (1968); (15) Busse (1970); (16) Glatzmaier & Gilman (1981); (17) Hindman & Jain (2022); (18) Hindman & Jain (2023).

Table 2. Overview of model assumptions used in the literature to compute eigenmodes.

publications	model assumptions	density stratification	differential rotation	buoyancy effects	latitudinal entropy gradient	super-adiabaticity
(5), (9)	compressible 2.5D	solar-like	solar-like	yes	yes	yes
(4), (11), (19)	anelastic 2.5D	solar-like	solar-like	yes	no	yes
(10), (20–21)	incompressible 2.5D	unstratified	no	no	no	no
(12), (16), (22)	sound-proof cylindrical	polytropic	no	yes	no	yes
(5), (7–8)	incompressible 1.5D (surface)	...	solar-like	no	no	no

References. The first 18 references are as listed in Table 1. Additional references: (19) Bhattacharya et al. (2024); (20) Rieutord & Valdettaro (1997); (21) Baruteau & Rieutord (2013); (22) Jain & Hindman (2023).

Notes. The notation 2.5D refers to a set of independent 2D (latitude-radius) problems, one for each azimuthal wavenumber m . The notation 1.5D refers to a set of independent 1D equations in latitude, one for each m .

Furthermore, Hanson et al. (2022) detected retrograde modes with equatorially-antisymmetric radial vorticity. They do not follow the dispersion relation of any classical Rossby modes. Since they propagate with phase speeds about three times that of the equatorial Rossby modes, they were called high-frequency retrograde (HFR) modes by Hanson et al. (2022). Many HFR modes also have critical latitudes as they propagate in the retrograde direction.

1.2. Linear models

Under the assumption that the modes have small enough amplitudes, linear modelling is key to identifying the modes and revealing their physical nature. It was understood early on that solar latitudinal differential rotation and turbulent viscosity are crucial ingredients to describe the purely toroidal modes on the sphere (Gizon et al. 2020b; Fournier et al. 2022). The frequency spectrum under differential rotation is significantly altered compared to the case of uniform rotation. Bekki et al. (2022b) also solved the eigenvalue problem in a spherical shell representative of the differentially rotating convection zone. The linear modes in 1.5D of Fournier et al. (2022) and 2.5D of Bekki et al. (2022b) were both essential in identifying the observed modes and providing a unified explanation for the equatorial Rossby and the mid- and high-latitude modes, including the $m = 1$ high-latitude mode (see Gizon et al. 2021, 2024). It was also found that the high-latitude modes are baroclinically unstable and are sensitive to the latitudinal entropy gradient in the convection zone. Linear modelling was also very useful in identifying the HFR modes as non-toroidal retrograde mixed inertial modes with anti-symmetric radial vorticity (Triana et al. 2022; Bhattacharya & Hanasoge 2023; Bekki 2024; Jain et al. 2024).

Furthermore, some linear studies have described retrograde modes that are similar to the equatorial Rossby modes but with $n = 1$, where n is the number of nodes in radius (Bekki et al.

2022b; Bhattacharya & Hanasoge 2023; Jain et al. 2024). These modes have been referred to as $n = 1$ equatorial Rossby modes (Bekki et al. 2022b). They also belong to the class of retrograde mixed modes, like the HFR modes, but with north-south symmetric radial vorticity (Bekki et al. 2022b; Jain et al. 2024). In order to label this particular subset of mixed modes, we stick to the name $n = 1$ equatorial Rossby mode. These modes have frequencies similar to the sectoral power of radial vorticity in the solar surface flows for $m \gtrsim 8$ (Hanson & Hanasoge 2024). However, the observed power cannot be conclusively attributed to these modes due to the lack of comparison between their eigenfunctions and the solar flow structures. Adding to that, the frequencies and growth rates of these linear modes are sensitive to the superadiabaticity, which is not well-constrained for the Sun (Hanson & Hanasoge 2024; Bekki et al. 2022b).

Linear calculations earlier predicted modes that are excited by thermal instability in a rotating fluid (Roberts 1968; Busse 1970). These are non-toroidal modes consisting of convective columns that propagate in the prograde direction under the effect of compressional and topographical β -effects (e.g., Glatzmaier & Gilman 1981; Gastine et al. 2014; Bekki et al. 2022b; Hindman & Jain 2022). They have been referred to using different names, such as columnar convective modes, Busse columns, banana cells, and thermal Rossby modes. In our paper, we refer to them as prograde columnar modes. In non-linear numerical simulations, prograde columnar modes play a crucial role in the dynamics of the convection zone as they transport angular momentum equatorward and contribute to determining the differential rotation profile (e.g., Miesch et al. 2006). They also transport heat poleward, which helps in establishing the thermal wind balance (e.g., Matilsky et al. 2020). Despite their important function in simulations, they have not yet been identified in the solar surface flows. There are several possible reasons why they have not been observed. They might be present below the near-surface layers but shielded by small-scale convection close to the solar

surface, or their spatial scale might be too small to be identified in the solar surface flows (Hindman & Jain 2022; Featherstone & Hindman 2016). Also, the modes may simply not be present to measurable amplitudes in the solar convection zone, which might be related to the unresolved convective conundrum (e.g., Hotta et al. 2023).

In our paper, we study the above-discussed modes as summarized in Table 1. Understanding the physics of inertial modes can help diagnose different properties of the solar interior to complement p mode helioseismology as they are sensitive to several parameters of the deep convection zone, including the turbulent viscosity, superadiabaticity, and latitudinal entropy gradient (Gizon et al. 2021; Bekki et al. 2022b; Hanson & Hanasoge 2024). More importantly, the baroclinically unstable high-latitude modes likely play a key role in the dynamics of the Sun by controlling the solar differential rotation (Bekki et al. 2024).

2. Previous theoretical studies: various assorted assumptions

Rieutord & Valdettaro (1997) numerically analysed the spectrum of inertial waves trapped in a spherical shell containing a uniformly rotating incompressible fluid. Baruteau & Rieutord (2013) extended this setup without stratification to a differentially rotating fluid. Following the discovery of solar quasi-toroidal inertial modes (Löptien et al. 2018; Gizon et al. 2021), several attempts were made to model the various classes of solar inertial modes employing varying simplifying assumptions. Bekki et al. (2022b) modelled the observed solar inertial modes using a differentially rotating compressible fluid in the solar convection zone. Furthermore, Bhattacharya & Hanasoge (2023); Bhattacharya et al. (2024) modelled the solar inertial modes in the spherical shell geometry considering the anelastic approximation (Glatzmaier & Gilman 1981). This assumes that the sound speed is much faster than the other characteristic flow speeds in the system, thereby filtering out the acoustic modes. Although these sound-proof setups often do not conserve energy for gravity waves in the sub-adiabatic radiative interior, they generally conserve energy in the nearly adiabatic convection zone (Brown et al. 2012). Triana et al. (2022) also used a simpler uniformly rotating unstratified incompressible fluid in a spherical shell to model the solar inertial modes. The study aimed to identify the HFR modes discovered in Hanson et al. (2022). Such an incompressible model is widely used to study planetary eigenmodes employing the Boussinesq approximation to include the buoyancy effects (e.g., Marti et al. 2016; Barik et al. 2023). Furthermore, there are several studies in simplified geometries such as on spherical surfaces (Fournier et al. 2022; Gizon et al. 2020b) and in cylindrical geometry (Jain & Hindman 2023; Jain et al. 2024). We refer to the model of Jain & Hindman (2023) as sound-proof because it considers the limit of low frequency and high sound speed to remove the sound waves.

The setups in these linear models for the solar inertial modes differ in various aspects, such as the numerical domain, the degree of superadiabaticity, the choice of background rotation profile, and the latitudinal entropy gradient in the convection zone. Many studies, including Triana et al. (2022), Bhattacharya & Hanasoge (2023), Jain & Hindman (2023) and Jain et al. (2024) assume solid body rotation for the Sun. However, as discussed earlier, latitudinal differential rotation implies the existence of critical latitudes and additional families of modes (e.g. the high-latitude modes). Table 2 summarizes the assorted fundamental model assumptions in the various linear simulations of the solar inertial modes. Although the solar inertial modes have also been

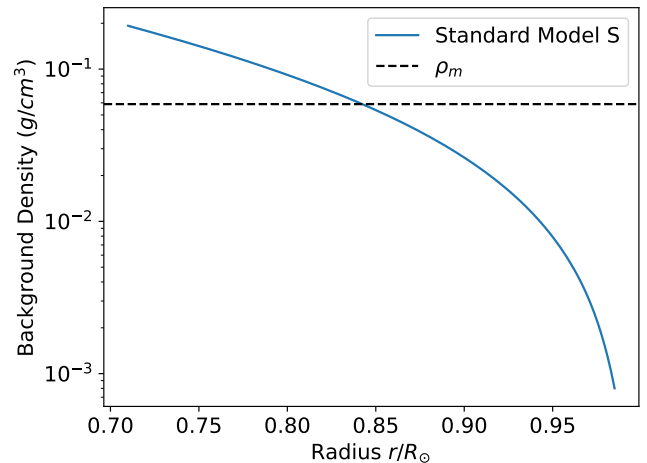


Fig. 1. Variation of the background density in the solar convection zone from the standard model S (Christensen-Dalsgaard et al. 1996), denoted by the blue curve. The black dashed line shows the mean density ρ_m in the solar convection zone. The mean density is used in the Boussinesq setup, while the other stratified setups use the density from model S.

studied using nonlinear simulations (e.g., Bekki et al. 2022a, 2024; Blume et al. 2024), we limit our studies to the linear modes in the solar convection zone.

Despite employing several differing simplifications, the effects of these simplifying assumptions on the linear inertial modes have not been tested. Bekki (2024) compared only the HFR modes obtained from the different models used in literature employing spherical shell geometry. The effects of various sound-proof approximations were tested earlier for the gravity waves in stellar interiors (Brown et al. 2012; Vasil et al. 2013), but not for inertial modes.

3. Description of our numerical computations: compressible, anelastic, and Boussinesq cases

In this work, we study the effects of the anelastic and Boussinesq approximations on the solar inertial modes by comparison to the fully compressible case used as the reference. We implement the compressible, anelastic and Boussinesq model setups in Dedalus (Burns et al. 2020) using the same boundary conditions (stress-free impenetrable). The background stratification is the same for the compressible and the anelastic cases. The background temperature, superadiabaticity, and latitudinal entropy variations are identical in all computations, including the Boussinesq case. This helps us understand the main physical ingredients needed to describe the inertial modes correctly. We note that we always represent the effects of small-scale turbulence in terms of turbulent eddy viscosity. The effects of magnetic fields on the inertial modes are also ignored. We discuss the five types of inertial modes described in Table 1.

3.1. Linearized equations of fluid dynamics

The linearized Navier-Stokes equation in the Carrington frame rotating at $\Omega_0/2\pi = 456$ nHz can be expressed as

$$\frac{\partial \mathbf{u}}{\partial t} + \mathbf{v}_0 \cdot \nabla \mathbf{u} + \mathbf{u} \cdot \nabla \mathbf{v}_0 + 2\Omega_0 \mathbf{e}_z \times \mathbf{u} + \nabla \left(\frac{p_1}{\rho_0} \right) - \frac{s_1}{c_p} g \mathbf{e}_r - \frac{1}{\rho_0} \nabla \cdot \overleftrightarrow{\mathbf{D}} = 0. \quad (1)$$

Here, \mathbf{u} , ρ_1 , p_1 , and s_1 are the perturbations of velocity, density, pressure, and entropy with respect to the background, while c_p is the specific heat at constant pressure. The viscous stress tensor is given by $\overleftrightarrow{D} = \rho_0 \nu \left(\nabla \mathbf{u} + \nabla \mathbf{u}^T - \frac{2}{3} (\nabla \cdot \mathbf{u}) \overleftrightarrow{I} \right)$, with $\nu = 10^{12} \text{ cm}^2/\text{s}$ being the spatially constant isotropic turbulent viscosity and \overleftrightarrow{I} the identity tensor. The background flow $\mathbf{v}_0 = (\Omega(r, \theta) - \Omega_0) r \sin \theta \mathbf{e}_\phi$ includes the solar differential rotation $\Omega(r, \theta)$ in the convection zone taken from Larson & Schou (2018). In this study, we omit the effects of meridional circulation, which is shown to have a small impact (Gizon et al. 2020b; Fournier et al. 2022). For compressible and anelastic setups, the background stratification of density ρ_0 , pressure p_0 , and temperature T_0 for the compressible and anelastic models are taken from the standard solar model S (Christensen-Dalsgaard et al. 1996). The acceleration due to gravity g is determined using the hydrostatic balance in model S. For the anelastic setup, Eq. (1) is the form of the Navier-Stokes equation that is recommended by Brown et al. (2012), as it conserves energy both in the convection zone and the radiative zone. For the incompressible setup, we consider the effects of buoyancy using the Boussinesq approximation in a similar manner to Spiegel & Veronis (1960), so that the model has a similar condition as the other models and allows baroclinic instability (e.g., Molemaker et al. 2005). This is in contrast to the model used in Triana et al. (2022), which ignored the buoyancy effects. Hence, we refer to it as the Boussinesq model instead of the incompressible model in our study. Under this approximation, we use the mean density, $\rho_m = 0.0589 \text{ g cm}^{-3}$, in the convection zone as the background density ρ_0 . Figure 1 depicts the difference between the mean density and the background density from model S. However, the temperature T_0 is used from the Solar model S. The background pressure p_0 is given by the hydrostatic equilibrium like in Spiegel & Veronis (1960). See Appendix A for more details.

The following linearized equation of entropy (s) is used

$$\frac{\partial s_1}{\partial t} + \mathbf{v}_0 \cdot \nabla s_1 + u_r \frac{\partial s_0}{\partial r} + \frac{u_\theta}{r} \frac{\partial s_0}{\partial \theta} - \frac{1}{\rho_0 T_0} \nabla \cdot (\kappa \rho_0 T_0 \nabla s_1) = 0, \quad (2)$$

where s_0 denotes the background entropy. In this study, we assume the adiabatic stratification in radius, $\partial s_0 / \partial r = 0$, for simplicity. The latitudinal entropy gradient $\partial s_0 / \partial \theta$ represents the thermal wind balance of the solar differential rotation and is estimated as (e.g., Pedlosky 1982; Thompson et al. 2003)

$$\frac{\partial s_0}{\partial \theta} = r^2 \sin \theta \frac{g}{c_p} \frac{\partial(\Omega^2)}{\partial z}, \quad (3)$$

where z is the coordinate along the rotational axis. The turbulent thermal diffusivity κ is assumed to be spatially constant and have the same value as ν .

For a compressible fluid, the linearized continuity equation is used

$$\frac{\partial \rho_1}{\partial t} + \nabla \cdot (\rho_0 \mathbf{u}) + \nabla \cdot (\rho_1 \mathbf{v}_0) = 0, \quad (\text{compressible}) \quad (4)$$

in combination with the linearized equation of state

$$\frac{p_1}{p_0} = \gamma \frac{\rho_1}{\rho_0} + \frac{s_1}{c_v}, \quad (5)$$

where $\gamma = 5/3$ is the specific heat ratio, and c_v is the specific heat at constant volume. Under the anelastic approximation, we assume that the sound speed is much faster than the rotational or

advective flow speed in the Sun. Thus, the continuity equation is reduced to the anelastic equation,

$$\nabla \cdot (\rho_0 \mathbf{u}) = 0. \quad (\text{anelastic}) \quad (6)$$

Under the Boussinesq approximation, this is further reduced to

$$\nabla \cdot \mathbf{u} = 0. \quad (\text{Boussinesq}) \quad (7)$$

The above linearized fluid dynamical equations are used in this work to model and understand the physics of solar inertial modes.

3.2. Boundary conditions

The Sun does not have any hard boundaries, but to execute the computations, one needs to implement some boundary conditions. Like some previous linear studies, we execute our computations in the spherical shell of the solar convection zone. The numerical domain in our study extends from the base of the convection zone ($r_i = 0.71 R_\odot$) to slightly below the photosphere ($r_o = 0.985 R_\odot$). There are various possible options for the boundary conditions, like free-surface boundary conditions, stress-free boundary conditions, and no-slip boundary conditions. It is not very clear which boundary condition would be the best for modelling the solar inertial modes. The no-slip boundary condition is not expected to be good in modelling the inertial modes as it does not allow any motions at the boundaries. The free-surface boundary condition might be adequate to model the inertial modes as it allows a flexible boundary height. However, to avoid the computational complexity, we use the stress-free impenetrable boundary conditions, which have been used in previous studies of the solar inertial modes (e.g., Bekki et al. 2022b; Bhattacharya et al. 2024; Triana et al. 2022). This works better than the no-slip boundary conditions as it allows horizontal motions at the boundaries, although it assumes no vertical motions at the boundaries. Also, we assume no flux of entropy across each boundary. The boundary conditions can be expressed as

$$u_r(r_i) = u_r(r_o) = 0, \quad (8)$$

$$\overleftrightarrow{D}_{r\theta}(r_i) = \overleftrightarrow{D}_{r\theta}(r_o) = 0, \quad (9)$$

$$\overleftrightarrow{D}_{r\phi}(r_i) = \overleftrightarrow{D}_{r\phi}(r_o) = 0, \quad (10)$$

$$\left. \frac{\partial s_1}{\partial r} \right|_{r_i} = \left. \frac{\partial s_1}{\partial r} \right|_{r_o} = 0. \quad (11)$$

Since we use spherical harmonics as basis functions, the problem has no singularity at the poles and requires no boundary conditions at the poles (Boyd 2001).

3.3. Formulation of eigenvalue problem in Dedalus

We use Dedalus (Burns et al. 2020), a flexible open-source spectral code, to solve the linear eigenvalue problem of the solar inertial modes. The above Eqs. (1), (2), and (4) – (7) are solved as an eigenvalue problem using the wave Ansatz where each perturbed physical quantity is proportional to $\exp(im\phi - i\omega t)$, with m the azimuthal order and ω the frequency. Equations (8) – (11) are implemented as the boundary conditions. The calculations are done on the spherical shell basis of Dedalus using the sparse eigenvalue solver (Burns et al. 2020). We solve the sparse problem spanning the range of the inertial frequencies, $|\Re[\omega]| \leq 2\Omega_0$. This helps us filter out the low-frequency modes of our interest. The obtained eigenfrequencies ω and eigenfunctions of the inertial modes are studied for different model assumptions. All the

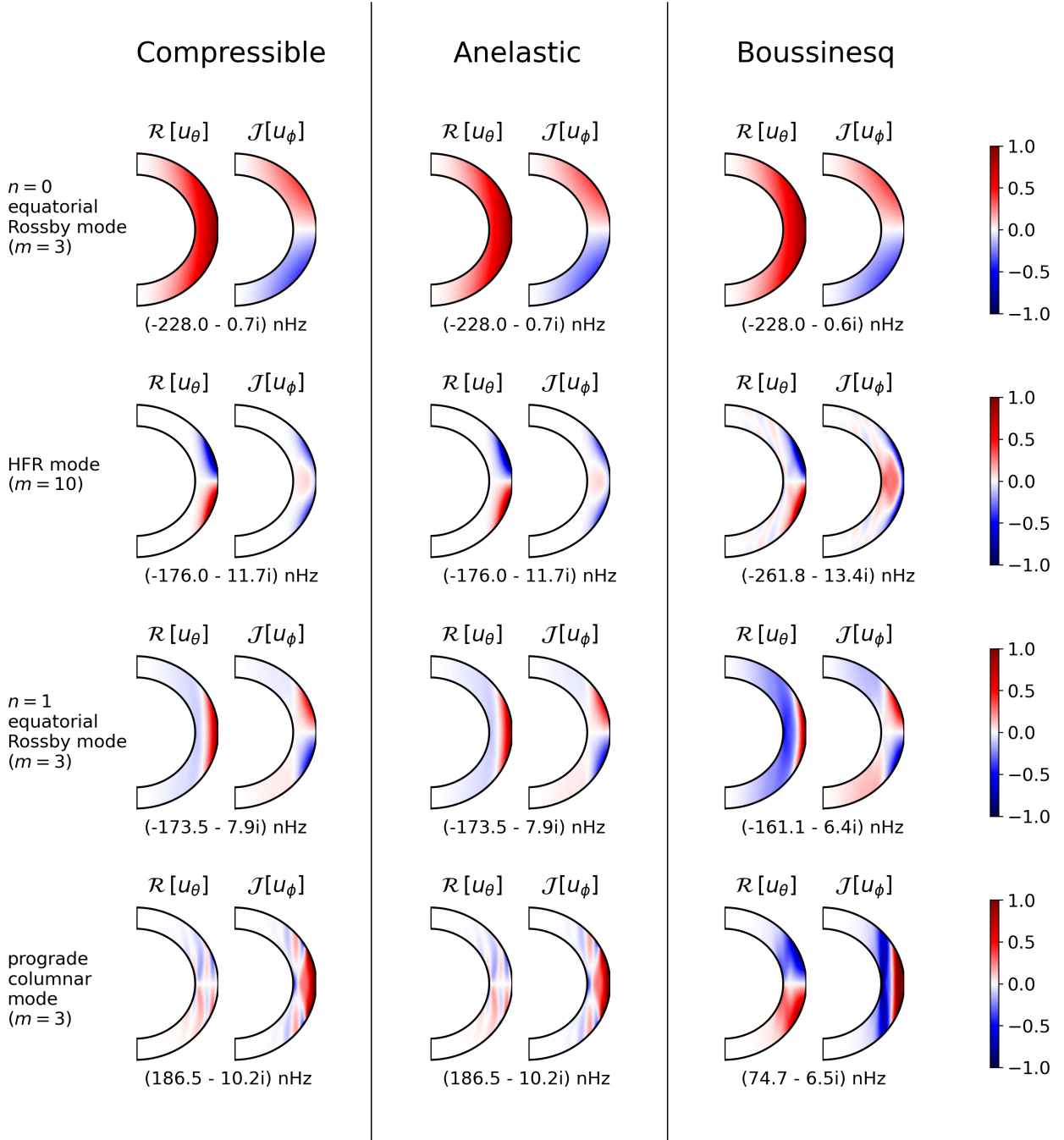


Fig. 2. Comparison of the eigenmodes of the different classes of inertial modes (see Table 1) computed using compressible, anelastic, and Boussinesq models under uniform rotation. Note that the unstable high-latitude inertial modes are absent under solid body rotation. Here, we plot the real part of u_θ and the imaginary part of u_ϕ of the computed eigenmodes. The longitudes corresponding to the real and imaginary phases of the eigenfunctions are $\phi = \phi_0$ and $\phi = \phi_0 - \pi/2m$, respectively, where ϕ_0 is a longitude with u_θ being maximum. The corresponding frequencies measured in the Carrington frame are stated below each eigenmode. The imaginary parts of the frequencies are the growth rates of the modes. All the eigenfunctions are normalized such that the maximum of u_θ is 1 m/s at the surface.

eigenmodes presented in this paper are obtained using a grid on the spherical shell basis with 24 radial and 124 latitudinal points. They are detected based on their north-south symmetries, growth rates, and other known properties, such as the number of radial or latitudinal nodes. The convergence errors in the eigenfrequencies obtained by halving or doubling the resolutions are several orders of magnitude lower than the frequency resolution of observations (which is on the order of a few nHz, see Gizon et al. 2021). The reported eigenfunctions are also well-converged.

4. Effects of simplifying the continuity equation

4.1. Effects of anelastic and Boussinesq approximations under uniform rotation

We start by comparing the eigenmodes obtained from the different models under uniform rotation. Figure 2 compares the eigenfunctions of the $n = 0$ equatorial Rossby mode with $m = 3$, the HFR mode with $m = 10$, the $n = 1$ equatorial Rossby mode with $m = 3$, and the prograde columnar mode with $m = 3$ for

the three different models. First, we note that the eigenmodes are almost identical for the compressible and anelastic models. They have negligible differences in the eigenfunctions of less than 1%, and their frequencies are the same correct up to 0.1 nHz. However, the eigenmodes obtained using the Boussinesq model differ significantly from those using the other models, except for the $n = 0$ equatorial Rossby modes. In all the models, the $n = 0$ equatorial Rossby modes are almost perfectly toroidal and are driven by the planetary β -effect, which is unaffected by the background density stratification. However, the other modes, having a substantial non-toroidal nature, are quite different in the Boussinesq model as compared to the other models. Significant differences seen in the spatial eigenfunctions of the HFR modes, the $n = 1$ equatorial Rossby modes, and the prograde columnar modes can be understood as follows: In contrast to the $n = 0$ equatorial Rossby modes, these non-toroidal modes have a radial node of the horizontal velocity eigenfunctions in the convection zone (CZ). Under the background density stratification, the constraint of local mass conservation (Eq. 6) requires the mass fluxes in the lower and upper parts of CZ (across the nodal plane) to be balanced with each other, leading to slower velocities in the lower CZ. In the Boussinesq model, on the other hand, the velocity eigenfunctions can have comparable amplitudes throughout the CZ.

Figure 3 exhibits the dispersion relations of the modes shown in Fig. 2 for the three models under uniform rotation for azimuthal orders m ranging from 0 to 15. Like the eigenmodes, the dispersion relations are identical for the anelastic and the compressible models for the various modes over all the values of m . The deviations in the dispersion relations of the Boussinesq model from the other models can be observed for the non-toroidal modes discussed above. The deviations are enormous for the prograde columnar modes and the HFR modes. In both cases, the frequencies are significantly shifted to a negative (more retrograde) direction. Having a less toroidal nature, the deviations are smaller for the $n = 1$ equatorial Rossby modes. The purely toroidal $n = 0$ equatorial Rossby modes have the same dispersion relations for all the models.

To understand the effects of using the Boussinesq approximation on mode frequencies, we examine the linearized vorticity equation. Taking a curl of Eq. (1) under uniform rotation, the radial and z components of the vorticity equation can be written as

$$\frac{\partial \zeta_r}{\partial t} \approx \underbrace{\frac{2\Omega_0 \sin \theta}{r} u_\theta}_{\text{planetary } \beta\text{-effect}} - \frac{2\Omega_0 \cos \theta}{H_\rho} u_r + 2\Omega_0 \cos \theta \frac{\partial u_r}{\partial r} - \frac{2\Omega_0 \sin \theta}{r} \frac{\partial u_r}{\partial \theta}, \quad (12)$$

$$\frac{\partial \zeta_z}{\partial t} \approx \underbrace{-\frac{2\Omega_0}{H_\rho} u_r}_{\text{compressional } \beta\text{-effect}} + \underbrace{2\Omega_0 \frac{\partial u_z}{\partial z}}_{\text{topographic } \beta\text{-effect}} - \frac{g}{c_p r} \frac{\partial s_1}{\partial \phi}, \quad (13)$$

where $\zeta = \nabla \times \mathbf{u}$ and H_ρ is the density scale height. The viscous diffusive terms are omitted for simplicity. Here, the first term on the right-hand side of the Eq. (12) represents the planetary β -effect and the first term on the right-hand side of the Eq. (13) represents the compressional β -effect. The second term on the right-hand side of the Eq. (13) corresponds to the topographic β -effect (when integrated over z). To assess the relative importance of these β -effects on the mode frequencies, we further transform

the above equations into the following form:

$$\omega |\zeta_r|^2 \approx \mathcal{G}_{\text{planetary}} + \mathcal{G}_{\text{comp}} + \mathcal{G}_{\text{other}}, \quad (14)$$

$$\omega |\zeta_z|^2 \approx \mathcal{W}_{\text{comp}} + \mathcal{W}_{\text{topographic}} + \mathcal{W}_{\text{other}}, \quad (15)$$

with

$$\mathcal{G}_{\text{planetary}} = i \frac{2\Omega_0 \sin \theta}{r} u_\theta \zeta_r^*, \quad (16)$$

$$\mathcal{G}_{\text{comp}} = -i \frac{2\Omega_0 \cos \theta}{H_\rho} u_r \zeta_r^*, \quad (17)$$

$$\mathcal{G}_{\text{other}} = 2i\Omega_0 \cos \theta \frac{\partial u_r}{\partial r} \zeta_r^* - i \frac{2\Omega_0 \sin \theta}{r} \frac{\partial u_r}{\partial \theta} \zeta_r^*, \quad (18)$$

and

$$\mathcal{W}_{\text{comp}} = -i \frac{2\Omega_0}{H_\rho} u_r \zeta_z^*, \quad (19)$$

$$\mathcal{W}_{\text{topographic}} = 2i\Omega_0 \frac{\partial u_z}{\partial z} \zeta_z^*, \quad (20)$$

$$\mathcal{W}_{\text{other}} = \frac{mg}{c_p r} s_1 \zeta_z^*. \quad (21)$$

Here, $*$ denotes the complex conjugate of the quantities. The real part of the quantities \mathcal{G} and \mathcal{W} being negative implies that the physical effect associated with the quantity promotes the retrograde propagation of the mode, while the real part being positive implies that it promotes the prograde propagation of the mode. Figures B.1 – B.4 show all the terms in the Eqs. (14) and (15) for the $n = 0$ equatorial Rossby mode with $m = 3$, the HFR mode with $m = 10$, the $n = 1$ equatorial Rossby mode with $m = 3$, and the prograde columnar mode with $m = 3$ from compressible and Boussinesq setups. Note that $\mathcal{G}_{\text{comp}} = \mathcal{W}_{\text{comp}} = 0$ in the Boussinesq setup as the density scale height H_ρ becomes infinite due to the assumption of constant density.

Our analysis reveals that the changes in the mode frequencies from the anelastic (or compressible) to Boussinesq models are predominantly caused by the absence of $\mathcal{W}_{\text{comp}}$ in the z -vorticity equation. Figure 4 shows $\mathcal{W}_{\text{comp}}$ in the compressible setup for the the HFR mode with $m = 10$, $n = 1$ equatorial Rossby mode with $m = 3$, and the prograde columnar mode with $m = 3$. As for the $n = 1$ equatorial Rossby modes, $\Re[\mathcal{W}_{\text{comp}}]$ is negative, suggesting that the compressional β -effect promotes their retrograde mode propagation. This is because, in these modes, the radial vortical motions are dominant and z -vorticity ζ_z is primarily generated by the strong radial shear of longitudinal flows and is not associated with their radial motions (ζ_z and $-\partial u_r / \partial \phi$ have the opposite sign). A disappearance of $\mathcal{W}_{\text{comp}}$ in the Boussinesq model thus leads to a slight shift of their mode frequencies towards the positive (more prograde) direction, as shown in Fig. 3 for $m \leq 4$. On the other hand, both HFR modes and the prograde columnar modes have strongly positive $\mathcal{W}_{\text{comp}}$, indicating that the compressional β -effect enforces their prograde propagation. This is because their radial motions are strongly associated with their z -vortices (ζ_z and $-\partial u_r / \partial \phi$ have the same sign). The absence of the compressional β -effect shifts the frequencies of the HFR modes and the prograde columnar modes towards the negative (more retrograde), as seen in Fig. 3. We also note that, in prograde columnar modes, the planetary β -effect plays an additional role in decreasing their prograde frequencies in the Boussinesq model (see Fig. B.4). Without density stratification, upflows are converged towards the equator due to the spherical curvature, which enhances the planetary β -effect. This does not occur in compressible or anelastic models because the upflows tend to expand and drive horizontally diverging motions due to the background density stratification.

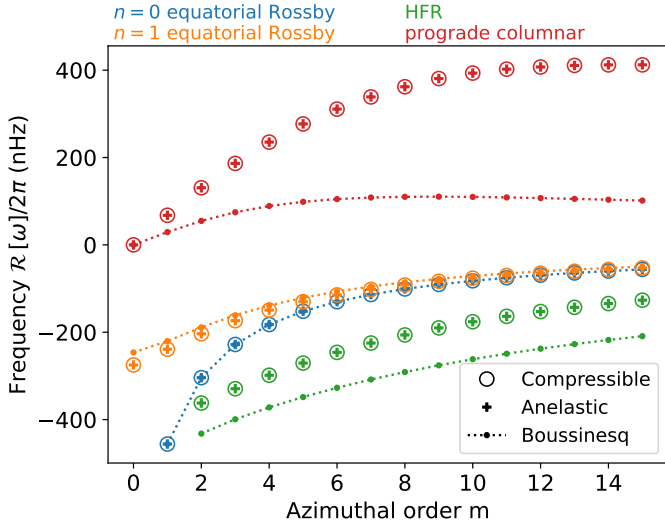


Fig. 3. Dispersion relations of the studied classes of inertial modes under uniform rotation for a range of azimuthal orders $0 \leq m \leq 15$. The blue, green, orange, and red colours represent the $n = 0$ equatorial Rossby, the HFR, the $n = 1$ equatorial Rossby, and the prograde columnar modes, respectively. Open circles, cross symbols, and dotted points show the results computed from the fully compressible, anelastic, and Boussinesq models, respectively.

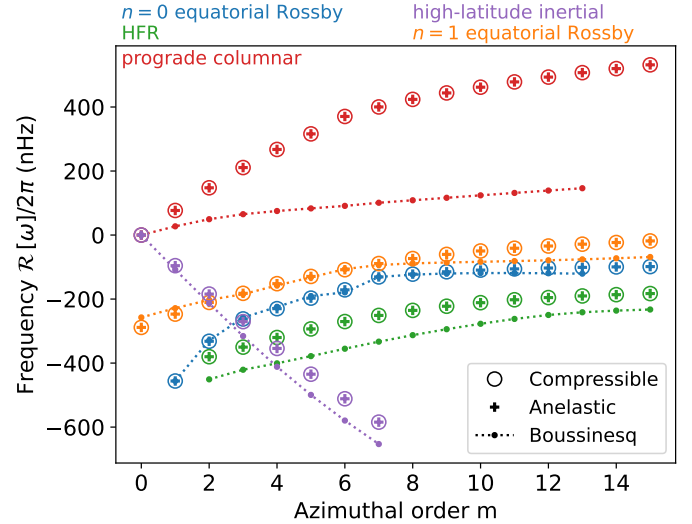


Fig. 5. Dispersion relations of the various classes of inertial modes in Table 1, obtained using the different models with solar differential rotation and associated latitudinal entropy gradient. The same notation is used for colours and symbols as in Fig. 3. The only addendum is the high-latitude mode with north-south symmetric radial vorticity, represented in purple.

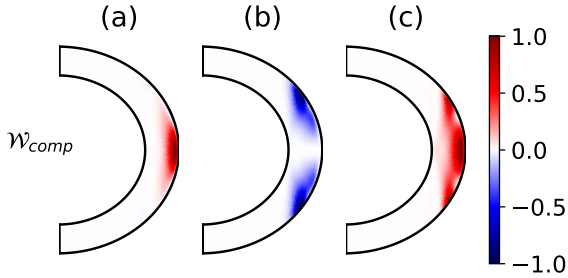


Fig. 4. Estimates of the importance of the compressional β -effect under uniform rotation using $\Re[\mathcal{W}_{\text{comp}}]$ defined in Eq. (19) for the compressible model. $\Re[\mathcal{W}_{\text{comp}}]$ being negative implies that the compressional β -effect promotes retrograde propagation, while it being positive implies that it promotes prograde propagation. Column (a) denotes the HFR mode with $m = 10$, column (b) denotes the $n = 1$ equatorial Rossby mode with $m = 3$, and column (c) denotes the prograde columnar mode with $m = 3$. For all the modes, $\Re[\mathcal{W}_{\text{comp}}]$ is normalized to have the maximum absolute value of 1.

4.2. Effects of anelastic and Boussinesq approximations under solar differential rotation and latitudinal entropy gradient

Now, we include solar differential rotation and its associated latitudinal entropy gradient in our computations. Figure 5 depicts the dispersion relations of the different modes with $0 \leq m \leq 15$ under this setup for all the models. Here, we additionally include the high-latitude modes, which are baroclinically unstable and thus owe their existence to the Sun's differential rotation and the latitudinal entropy gradient (Bekki et al. 2022b). For simplicity, we only study the high-latitude modes with north-south symmetric radial vorticity. Like the uniform rotation case, the compressible and anelastic models have the same dispersion relations for the different modes. In the Boussinesq model, the frequencies of the prograde columnar modes and the HFR modes are both shifted towards the negative direction (more

retrograde). In contrast, the frequencies of the $n = 0$ equatorial Rossby and the $n = 1$ equatorial Rossby modes are only marginally changed. These results are consistent with the uniform rotation case (§ 4.1). The retrograde-propagating high-latitude modes exhibit a trend of the negative frequency shift similar to that of the HFR modes. This can also be understood as a consequence of the absence of the compressional β -effect in the Boussinesq model because the high-latitude modes are essentially non-toroidal.

Figure 6 compares the velocity eigenfunctions of the $n = 0$ equatorial Rossby mode with $m = 3$, the high-latitude mode with $m = 1$, the HFR mode with $m = 10$, the $n = 1$ equatorial Rossby mode with $m = 3$, and the prograde columnar mode with $m = 3$ of the differentially-rotating case for the three different models. Again, the eigenmodes obtained from the compressible and anelastic models are found to be identical. This time, unlike the uniform rotation case, the eigenfunctions in the Boussinesq model are different even for the $n = 0$ equatorial Rossby modes. We note that under differential rotation $\Delta\Omega(r, \theta) = \Omega(r, \theta) - \Omega_0$, the critical latitudes θ_c are present in modes where the mode phase speeds match the local differential rotation speed, i.e., $\Delta\Omega(r, \theta_c) = \Re[\omega]/m$. The locations of the critical latitudes are denoted by black solid curves in Fig. 6. It is shown that the mode eigenfunctions are strongly distorted near the critical latitudes (Gizon et al. 2020b; Fournier et al. 2022). The $n = 0$ equatorial Rossby modes, the HFR modes, and the $n = 1$ equatorial Rossby modes are confined in the equatorial region by the critical latitudes. In contrast, the high-latitude modes exist in latitudes higher than the critical latitudes. The columnar modes are prograde-propagating and do not possess critical latitudes.

It is known that, under differential rotation, substantial radial motions tend to be driven near the critical latitudes (Bekki et al. 2022b). To estimate the relative impact of the radial motions on the mode eigenfunctions, we define the non-toroidicity Γ based on the ratio of the kinetic energy in the radial direction to the

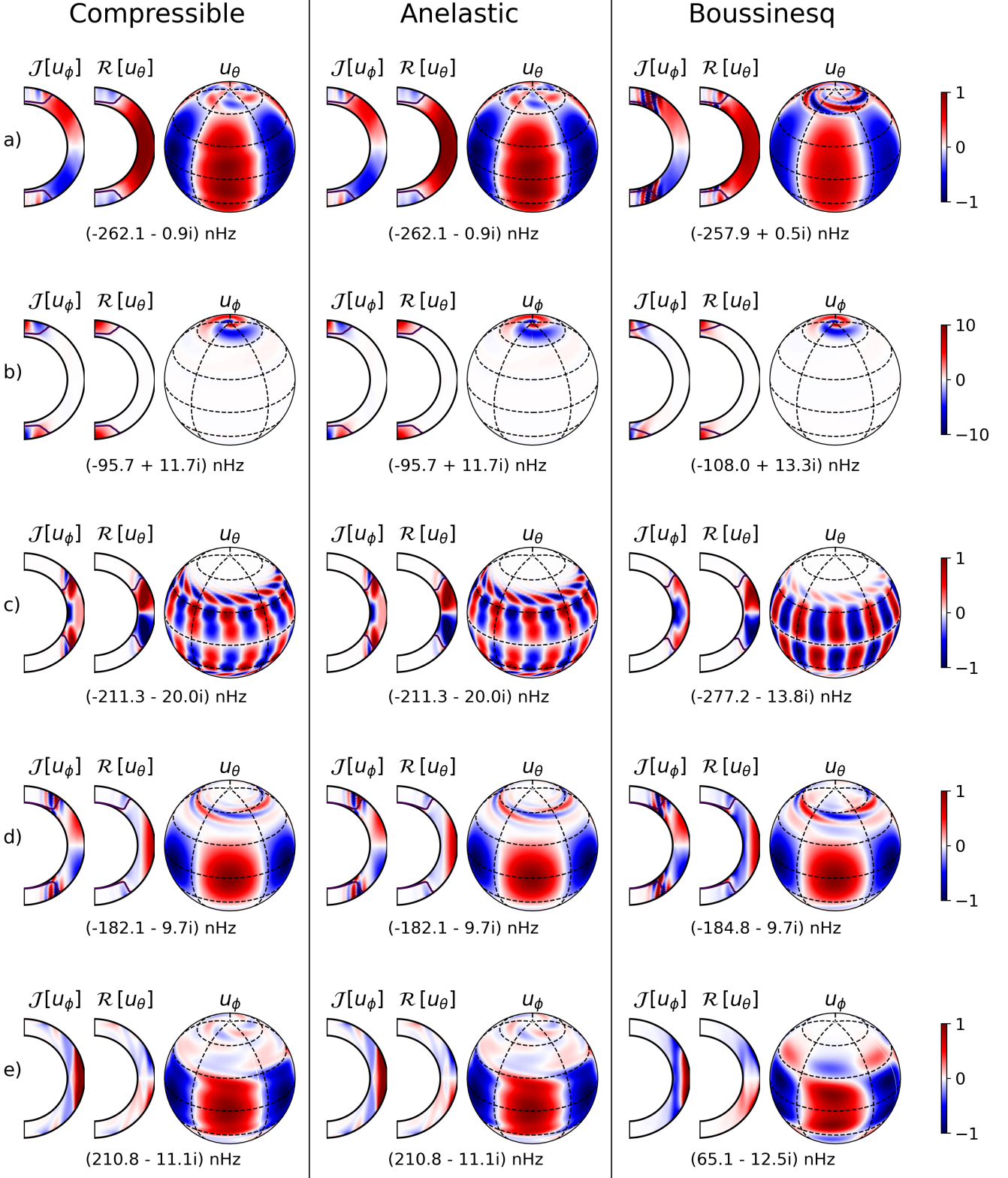


Fig. 6. Comparison between the eigenmodes of the different classes of inertial modes computed with compressible, anelastic, and Boussinesq models under solar differential rotation and its associated latitudinal entropy gradient. The different rows denote a) $n = 0$ equatorial Rossby mode ($m = 3$), b) high-latitude mode with north-south symmetric radial vorticity ($m = 1$), c) HFR mode ($m = 10$), d) $n = 1$ equatorial Rossby mode ($m = 3$), e) prograde columnar mode ($m = 3$). Here, we plot the real part of u_θ and the imaginary part of u_ϕ of the computed eigenmodes in the meridional plane. The corresponding longitudes are the same as in Fig. 2. We also plot the surface velocity u_ϕ for the high-latitude mode and the prograde columnar mode and u_θ for the other modes. The corresponding frequencies in the Carrington frame are stated below each eigenmode. The imaginary parts of the frequencies are the growth rates of the modes. All the eigenfunctions, except the high-latitude mode, are normalized such that the maximum of u_θ is 1 m/s at the surface. The high-latitude mode is set to have a maximum velocity of 10 m/s at the surface. The solid curves on the meridional cross-sections denote the critical latitude where $\Re[\omega] = m(\Omega - \Omega_0)$.

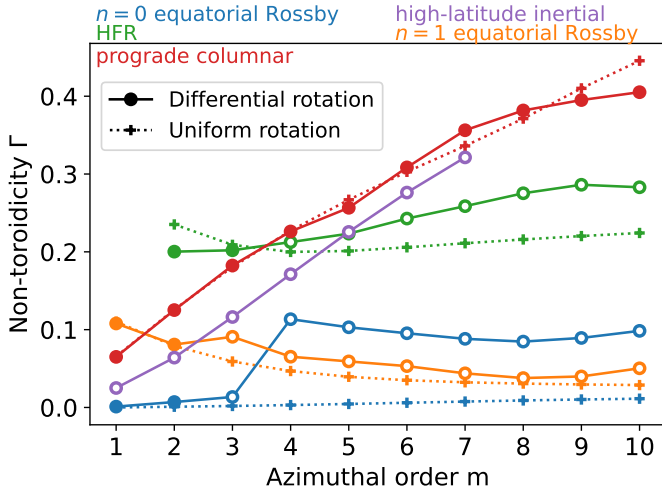


Fig. 7. Estimates of the importance of the radial motions associated with the different inertial modes using non-toroidicity Γ defined in Eq. (22) for the compressible setup. The values of non-toroidicity of the different modes are plotted against azimuthal orders ranging from $m = 1$ to $m = 10$. Different colours denote different modes, as in Fig. 5. The solid lines denote the modes under differential rotation, while the dotted lines denote the modes under uniform rotation. The open circles denote the modes affected by the critical latitudes under differential rotation, while the filled circles denote the other modes under differential rotation.

total kinetic energy of the mode:

$$\Gamma = \sqrt{\frac{\int_{CZ} \rho_0 u_r^2 dV}{\int_{CZ} \rho_0 (u_r^2 + u_\theta^2 + u_\phi^2) dV}}. \quad (22)$$

Figure 7 shows the non-toroidicity Γ of the various modes for different azimuthal orders m . It is shown that, compared to the uniform rotation case, the mode non-toroidicity Γ is significantly increased by the critical latitudes under differential rotation. This is most significant for the $n = 0$ equatorial Rossby modes at $m \geq 4$ but is also seen in the HFR modes ($m \geq 4$) and the $n = 1$ equatorial Rossby modes ($m \geq 3$). The non-toroidicity Γ increases almost linearly with m for the prograde columnar and high-latitude modes. Unlike the prograde columnar modes, the retrograde high-latitude modes are strongly influenced by the critical latitudes. In the Boussinesq model, they have more retrograde frequencies due to the absence of compressional β -effect. This causes their critical latitudes to shift to higher latitudes, leading to the confinement of the mode power at much higher latitudes than in the compressible model (see Fig. 6).

5. Summary and outlook

In this work, we used a fixed framework in Dedalus to assess the validity of the anelastic and Boussinesq approximations for modelling the inertial modes in the solar convection zone. Firstly, we find that the eigenmodes obtained by the compressible and anelastic models are almost identical, regardless of the presence of the background solar differential rotation. The anelastic assumption does not affect the properties of the solar inertial modes since a scale separation between low-frequency inertial modes and very high-frequency sound waves is achieved. Hence, one can safely use the anelastic approximation to simplify the calculations and reduce the numerical cost. Further,

our results show that most of the inertial modes computed using the Boussinesq model are appreciably different from those calculated using the other models. The Boussinesq model produces identical inertial modes as the other models only for the $n = 0$ equatorial Rossby modes under uniform rotation, which are purely toroidal. Otherwise, the absence of density stratification causes significant differences in non-toroidal modes in the Boussinesq model, which lacks the compressional β -effect.

There are still some issues remaining in the current modelling of the inertial modes. One prominent issue is the absence of the radiative interior below and the near-surface layer above the computational domain. Whether the anelastic formulation is valid for modelling the inertial modes in the radiative zone is an open problem. It is known that the anelastic models fail to conserve energy for the gravity waves in the sub-adiabatic radiative interior, and pseudo-incompressible models work better in such cases (Brown et al. 2012; Vasil et al. 2013). Thus, the anelastic approximation can likely affect the non-toroidal inertial modes in the radiative interior if they couple with gravity modes (gravito-inertial modes, see, e.g., Mathis 2009; Dintrans & Rieutord 2000). Nonetheless, the anelastic formulation used in our paper is expected to work in studying quasi-toroidal inertial modes in the radiative interior, as done through nonlinear numerical simulations (Blume et al. 2024). On the other hand, it is well known that the anelastic approximation breaks down when modelling the solar convection in the near-surface layer where the stratification becomes strongly superadiabatic and the convective speed becomes as high as the sound speed (e.g., Nordlund et al. 2009). The extent to which the anelastic formulation can be used to model the low-frequency inertial modes in this near-surface layer needs to be checked in the future.

Acknowledgements. Author contributions: LG and XZ initiated this project, SM implemented all the equations in Dedalus and performed the computations, YB provided close supervision to validate the results, all authors discussed the results, SM wrote the initial draft, and all authors contributed to the final manuscript. We thank R. Cameron, P. Dey, V. Kannan, and J. Schou for helpful discussions. We also acknowledge the hospitality of Nordita, Stockholm, during the 2024 program on stellar convection. SM is a member of the International Max Planck Research School for Solar System Science at the University of Göttingen. YB and LG acknowledge support from ERC Synergy Grant WHOLE SUN 810218. XZ acknowledges the financial support from the German Research Foundation (DFG) through grants 521319293, 540422505, and 550262949. The codes and data used in the manuscript are available in the Edmond database at <https://doi.org/10.17617/3.NP26A1>.

References

- Barik, A., Triana, S. A., Calkins, M., Stanley, S., & Aurnou, J. 2023, *Earth and Space Science*, 10, e2022EA002606
- Baruteau, C. & Rieutord, M. 2013, *Journal of Fluid Mechanics*, 719, 47
- Bekki, Y. 2024, *A&A*, 682, A39
- Bekki, Y., Cameron, R. H., & Gizon, L. 2022a, *A&A*, 666, A135
- Bekki, Y., Cameron, R. H., & Gizon, L. 2022b, *A&A*, 662, A16
- Bekki, Y., Cameron, R. H., & Gizon, L. 2024, *Science Advances*, 10, eadk5643
- Bhattacharya, J. & Hanasoge, S. M. 2023, *ApJS*, 264, 21
- Bhattacharya, J., Hanson, C. S., Hanasoge, S. M., & Sreenivasan, K. R. 2024, *ApJ*, 965, 55
- Blume, C. C., Hindman, B. W., & Matilsky, L. I. 2024, *ApJ*, 966, 29
- Boyd, J. P. 2001, *Chebyshev and Fourier Spectral Methods* (Courier Corporation)
- Brown, B. P., Vasil, G. M., & Zweibel, E. G. 2012, *ApJ*, 756, 109
- Burns, K. J., Vasil, G. M., Oishi, J. S., Lecoanet, D., & Brown, B. P. 2020, *Physical Review Research*, 2, 023068
- Busse, F. H. 1970, *Journal of Fluid Mechanics*, 44, 441
- Christensen-Dalsgaard, J. 2002, *Reviews of Modern Physics*, 74, 1073
- Christensen-Dalsgaard, J., Dappen, W., Ajukov, S. V., et al. 1996, *Science*, 272, 1286
- Dintrans, B. & Rieutord, M. 2000, *A&A*, 354, 86
- Featherstone, N. A. & Hindman, B. W. 2016, *ApJ*, 818, 32

- Fournier, D., Gizon, L., & Hyst, L. 2022, A&A, 664, A6
- Gastine, T., Heimpel, M., & Wicht, J. 2014, Physics of the Earth and Planetary Interiors, 232, 36
- Giles, P. M., Duvall, T. L., Scherrer, P. H., & Bogart, R. S. 1997, Nature, 390, 52
- Gizon, L., Bekki, Y., Birch, A. C., et al. 2024, in IAU Symposium, Vol. 365, IAU Symposium, ed. A. V. Getling & L. L. Kitchatinov, 207–221
- Gizon, L., Cameron, R. H., Bekki, Y., et al. 2021, A&A, 652, L6
- Gizon, L., Cameron, R. H., Pourabdian, M., et al. 2020a, Science, 368, 1469
- Gizon, L., Fournier, D., & Albekioni, M. 2020b, A&A, 642, A178
- Glatzmaier, G. A. & Gilman, P. A. 1981, ApJS, 45, 335
- Greenspan, H. P. 1969, The theory of rotating fluids. (Cambridge University Press)
- Hanson, C. S. & Hanasoge, S. 2024, Physics of Fluids, 36, 086626
- Hanson, C. S., Hanasoge, S., & Sreenivasan, K. R. 2022, Nature Astronomy, 6, 708
- Hathaway, D. H., Upton, L., & Colegrove, O. 2013, Science, 342, 1217
- Hindman, B. W. & Jain, R. 2022, ApJ, 932, 68
- Hindman, B. W. & Jain, R. 2023, ApJ, 943, 127
- Hotta, H., Bekki, Y., Gizon, L., Noraz, Q., & Rast, M. 2023, Space Sci. Rev., 219, 77
- Jain, R. & Hindman, B. W. 2023, ApJ, 958, 48
- Jain, R., Hindman, B. W., & Blume, C. 2024, ApJ, 965, L8
- Larson, T. P. & Schou, J. 2018, Sol. Phys., 293, 29
- Liang, Z.-C. & Gizon, L. 2024, A&A, accepted, arXiv:2409.06896
- Liang, Z.-C., Gizon, L., Birch, A. C., & Duvall, T. L. 2019, A&A, 626, A3
- Liang, Z.-C., Gizon, L., Birch, A. C., Duvall, T. L., & Rajaguru, S. P. 2018, A&A, 619, A99
- Löptien, B., Gizon, L., Birch, A. C., et al. 2018, Nature Astronomy, 2, 568
- Marti, P., Calkins, M. A., & Julien, K. 2016, Geochemistry, Geophysics, Geosystems, 17, 3031
- Mathis, S. 2009, A&A, 506, 811
- Matilsky, L. I., Hindman, B. W., & Toomre, J. 2020, ApJ, 898, 111
- Miesch, M. S., Brun, A. S., & Toomre, J. 2006, ApJ, 641, 618
- Molemaker, M. J., McWilliams, J. C., & Yavneh, I. 2005, Journal of Physical Oceanography, 35, 1505
- Nordlund, Å., Stein, R. F., & Asplund, M. 2009, Living Reviews in Solar Physics, 6, 2
- Pedlosky, J. 1982, Geophysical fluid dynamics (New York: Springer-Verlag)
- Proxauf, B., Gizon, L., Löptien, B., et al. 2020, A&A, 634, A44
- Rieutord, M. & Valdettaro, L. 1997, Journal of Fluid Mechanics, 341, 77
- Roberts, P. H. 1968, Philosophical Transactions of the Royal Society of London Series A, 263, 93
- Schou, J., Antia, H. M., Basu, S., et al. 1998, ApJ, 505, 390
- Spiegel, E. A. & Veronis, G. 1960, ApJ, 131, 442
- Thompson, M. J., Christensen-Dalsgaard, J., Miesch, M. S., & Toomre, J. 2003, ARA&A, 41, 599
- Triana, S. A., Guerrero, G., Barik, A., & Requier, J. 2022, ApJ, 934, L4
- Vallis, G. K. 2006, Atmospheric and Oceanic Fluid Dynamics (Cambridge University Press)
- Vasil, G. M., Lecoanet, D., Brown, B. P., Wood, T. S., & Zweibel, E. G. 2013, ApJ, 773, 169

Appendix A: Sets of equations for the different models

Since there are subtle differences in the equations for the different models, we explicitly state the equations for the different models. The terms in the equations below have been explained in § 3.

Appendix A.1: Compressible model

The complete set of linearized equations for the compressible model are:

$$\frac{\partial \mathbf{u}}{\partial t} + \mathbf{v}_0 \cdot \nabla \mathbf{u} + \mathbf{u} \cdot \nabla \mathbf{v}_0 + 2\Omega_0 \mathbf{e}_z \times \mathbf{u} + \nabla \left(\frac{p_1}{\rho_0} \right) - \frac{s_1}{c_p} g \mathbf{e}_r - \frac{1}{\rho_0} \nabla \cdot \left(\rho_0 \nu \left(\nabla(\mathbf{u}) + \nabla(\mathbf{u}^T) - \frac{2}{3} (\nabla \cdot \mathbf{u}) \overleftrightarrow{\mathbf{I}} \right) \right) = 0, \quad (\text{A.1})$$

$$\frac{\partial s_1}{\partial t} + \mathbf{v}_0 \cdot \nabla s_1 + u_r \frac{\partial s_0}{\partial r} + \frac{u_\theta}{r} \frac{\partial s_0}{\partial \theta} - \frac{1}{\rho_0 T_0} \nabla \cdot (\kappa \rho_0 T_0 \nabla s_1) = 0, \quad (\text{A.2})$$

$$\frac{\partial \rho_1}{\partial t} + \nabla \cdot (\rho_0 \mathbf{u}) + \nabla \cdot (\rho_1 \mathbf{v}_0) = 0, \quad (\text{A.3})$$

$$\frac{p_1}{p_0} = \gamma \frac{\rho_1}{\rho_0} + \frac{s_1}{c_v}. \quad (\text{A.4})$$

For the compressible model, we solve for Eqs. (A.1)–(A.3) with the constraint Eq. (A.4).

Appendix A.2: Anelastic approximation

We use the type of anelastic formulation, which conserves energy in both the convection and radiative zones and is recommended by Brown et al. (2012). Following are the linearized equations for the anelastic model:

$$\frac{\partial \mathbf{u}}{\partial t} + \mathbf{v}_0 \cdot \nabla \mathbf{u} + \mathbf{u} \cdot \nabla \mathbf{v}_0 + 2\Omega_0 \mathbf{e}_z \times \mathbf{u} + \nabla \left(\frac{p_1}{\rho_0} \right) - \frac{s_1}{c_p} g \mathbf{e}_r - \frac{1}{\rho_0} \nabla \cdot \left(\rho_0 \nu \left(\nabla(\mathbf{u}) + \nabla(\mathbf{u}^T) - \frac{2}{3} (\nabla \cdot \mathbf{u}) \overleftrightarrow{\mathbf{I}} \right) \right) = 0, \quad (\text{A.5})$$

$$\frac{\partial s_1}{\partial t} + \mathbf{v}_0 \cdot \nabla s_1 + u_r \frac{\partial s_0}{\partial r} + \frac{u_\theta}{r} \frac{\partial s_0}{\partial \theta} - \frac{1}{\rho_0 T_0} \nabla \cdot (\kappa \rho_0 T_0 \nabla s_1) = 0, \quad (\text{A.6})$$

$$\nabla \cdot (\rho_0 \mathbf{u}) = 0. \quad (\text{A.7})$$

In this case, we solve for Eqs. (A.5)–(A.6), with the anelastic constraint Eq. (A.7). In the Navier-Stokes equation, we implicitly assume that it follows the equation of state (A.4), but we do not use it as an additional constraint while solving the eigenvalue problem.

Appendix A.3: Boussinesq approximation

Coming to the Boussinesq model, the linearized model equations are:

$$\frac{\partial \mathbf{u}}{\partial t} + \mathbf{v}_0 \cdot \nabla \mathbf{u} + \mathbf{u} \cdot \nabla \mathbf{v}_0 + 2\Omega_0 \mathbf{e}_z \times \mathbf{u} + \frac{1}{\rho_m} \nabla p_1 - \frac{s_1}{c_p} g \mathbf{e}_r - \nabla \cdot \left(\nu \left(\nabla(\mathbf{u}) + \nabla(\mathbf{u}^T) \right) \right) = 0, \quad (\text{A.8})$$

$$\frac{\partial s_1}{\partial t} + \mathbf{v}_0 \cdot \nabla s_1 + \frac{u_\theta}{r} \frac{\partial s_0}{\partial \theta} - \frac{1}{T_0} \nabla \cdot (\kappa T_0 \nabla s_1) = 0, \quad (\text{A.9})$$

$$\nabla \cdot \mathbf{u} = 0. \quad (\text{A.10})$$

Here, we again solve for Eqs. (A.8)–(A.9) with the incompressibility constraint Eq. (A.10). Here, ρ_m is the mean density of the solar convection zone from the Solar model S (see Fig. 1). Unlike Triana et al. (2022), we include the Boussinesq approximation, which considers the effect of density perturbations only in the buoyancy force term. The equations for the Boussinesq approximation are derived for a compressible fluid following similar procedures as Spiegel & Veronis (1960).

We use the same background temperature T_0 , which is almost adiabatic in the convection zone and taken from model S, for all three models. We consider no deviation from the adiabatic temperature gradient for simplicity and to match the conditions on all the models. We also use the same latitudinal entropy gradient from thermal wind balance in all three models, given by

$$\frac{\partial s_0}{\partial \theta} = r^2 \sin \theta \frac{g}{c_p} \frac{\partial(\Omega^2)}{\partial z}. \quad (\text{A.11})$$

Appendix B: Analysis of linearized vorticity equation for the inertial modes

In this appendix, we report detailed analyses of the terms in the radial and z vorticity equations (Eqs. (14) and (15)). Figure B.1 compares the significance of the left and right-hand side terms of the linearized vorticity equations for the $n = 0$ equatorial Rossby modes with $m = 3$ from the compressible and Boussinesq models under uniform rotation. The planetary β -effect represented by $\mathfrak{R}[\mathcal{G}_{\text{planetary}}]$ drives the retrograde propagation of these modes. Since the $n = 0$ equatorial Rossby modes are toroidal under uniform rotation, no difference is observed between the compressible and Boussinesq results. Figure B.2 shows the results for the $m = 10$ HFR mode. It implies that the retrograde propagation of the HFR modes is driven by combined effects of $\mathcal{G}_{\text{planetary}}$, $\mathcal{G}_{\text{comp}}$, $\mathcal{G}_{\text{other}}$, and $\mathcal{W}_{\text{topographic}}$. The radial motions associated with the z -vorticity give rise to the compressional β -effect $\mathfrak{R}[\mathcal{W}_{\text{comp}}]$, which acts against the other terms and promotes their prograde propagation. In the Boussinesq model, the mode frequencies become more retrograde due to the absence of $\mathcal{W}_{\text{comp}}$. Figure B.3 shows the results for the $n = 1$ equatorial Rossby mode with $m = 3$. In contrast to the $n = 0$ equatorial Rossby mode, the $n = 1$ equatorial Rossby mode contains both radial and z vortical motions. For the radial component of the vorticity ζ_r , the planetary β -effect is the primary driver of their retrograde propagation. It is also shown that the topographic β -effect represented by $\mathfrak{R}[\mathcal{W}_{\text{topographic}}]$ enhances the retrograde propagation of their z -vorticity ζ_z . In the Boussinesq model, the mode frequencies

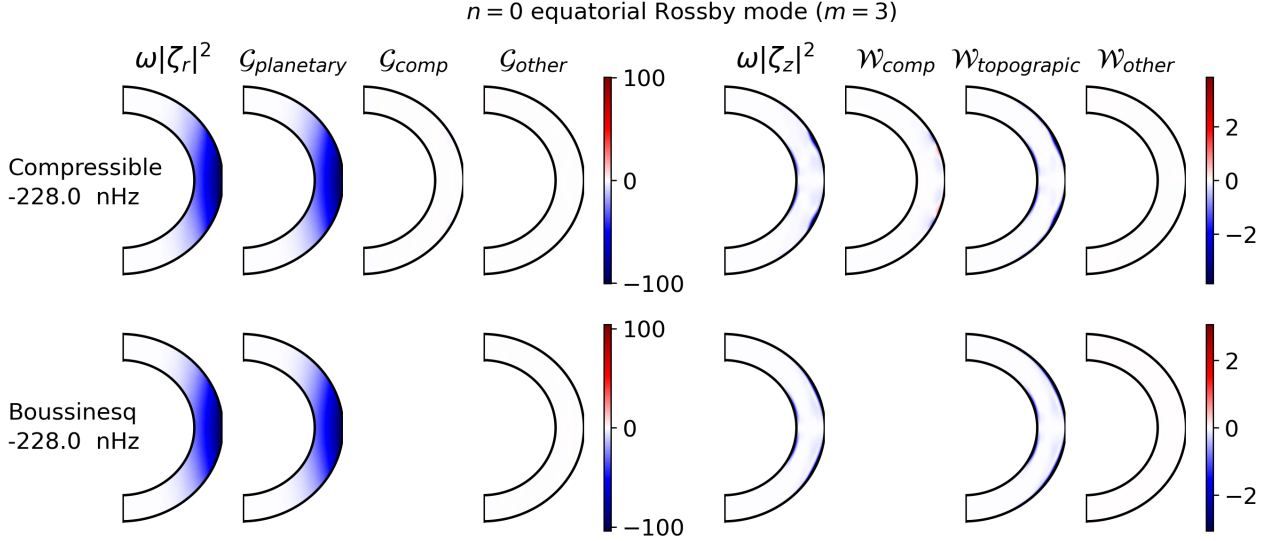


Fig. B.1. Relative importance of planetary β -effect ($\Re[\mathcal{G}_{\text{planetary}}]$), compressional β -effect ($\Re[\mathcal{G}_{\text{comp}}]$, $\Re[\mathcal{W}_{\text{comp}}]$), topographical β -effect ($\Re[\mathcal{W}_{\text{topographic}}]$) and other terms in the vorticity equation to determine the propagation and frequency of the $n = 0$ equatorial Rossby mode ($m = 3$) in the compressible and the Boussinesq models, under uniform rotation. Refer to Eqs. (16) - (21) for the definition of the various quantities. A quantity being negative implies that the associated physical effect promotes retrograde propagation, while it being positive implies that its physical effect promotes prograde propagation. The respective frequencies of the modes are specified on the left. The eigenfunctions from the different models are normalized to have the same integrated kinetic energy density such that the maximum absolute value of $\Re[\omega|\zeta_r|^2]$ is 100 for the compressible model.

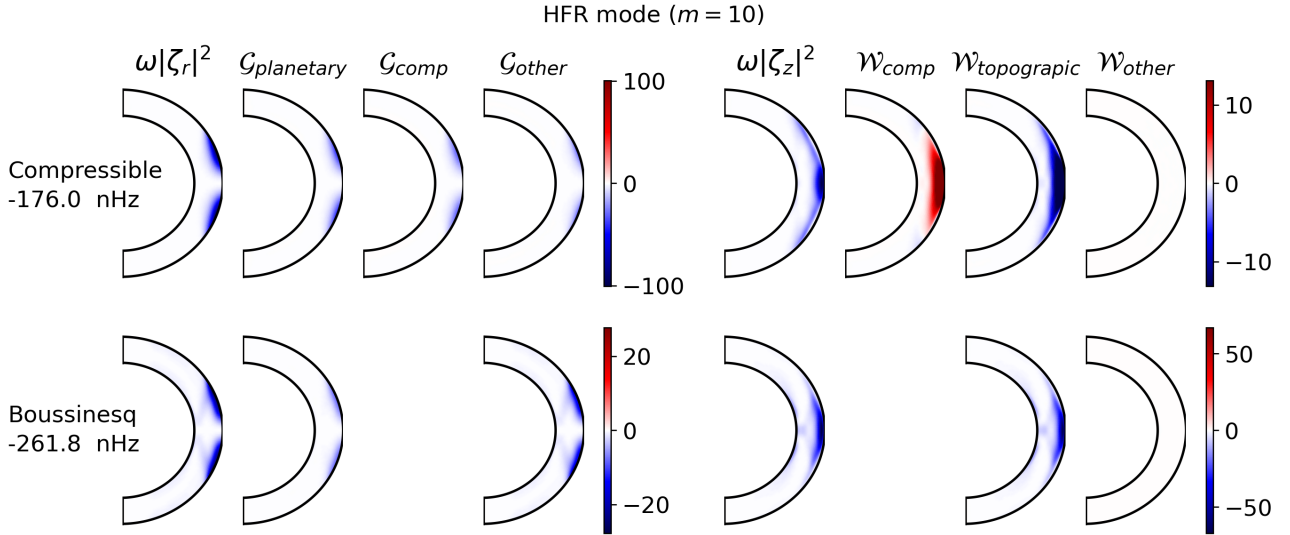


Fig. B.2. Relative importance of planetary β -effect ($\Re[\mathcal{G}_{\text{planetary}}]$), compressional β -effect ($\Re[\mathcal{G}_{\text{comp}}]$, $\Re[\mathcal{W}_{\text{comp}}]$), topographical β -effect ($\Re[\mathcal{W}_{\text{topographic}}]$) and other terms in the vorticity equation to determine the propagation and frequency of the HFR mode ($m = 10$) in the compressible and the Boussinesq models, under uniform rotation. The different quantities have the same definition and interpretation as in Fig. B.1. The respective frequencies of the modes are specified on the left. The eigenfunctions have the same normalization as in Fig. B.1.

become slightly more prograde due to the absence of the retrograde promoting $\mathcal{W}_{\text{comp}}$. Figure B.4 shows the results for the $m = 3$ prograde columnar mode. The z -vortical motions are much more dominant compared to the radial-vortical motions in these modes. In the compressible model, their prograde propagation is strongly driven by the compressional β -effect represented by $\Re[\mathcal{W}_{\text{comp}}]$ and weakly by the topographic β -effect represented by $\Re[\mathcal{W}_{\text{topographic}}]$. In the Boussinesq model, the only driving source for their prograde propagation is $\Re[\mathcal{W}_{\text{topographic}}]$. Furthermore, the absence of diverging (converging) tendency of upflows (downflows) enhances the radial vortical motions at the surface and consequently the planetary β -effect $\Re[\mathcal{G}_{\text{planetary}}]$,

which promotes the retrograde mode propagation. Therefore, the frequencies of the prograde columnar modes are strongly decreased in the Boussinesq model, as shown in Fig. 3.

Appendix C: Quantitative comparison of anelastic and Boussinesq models with respect to compressible model

The following Tables C.1 – C.4 present the frequencies ω and non-toroidicity Γ of different modes under uniform rotation for the three models. Tables C.5 – C.9 report the same for the modes

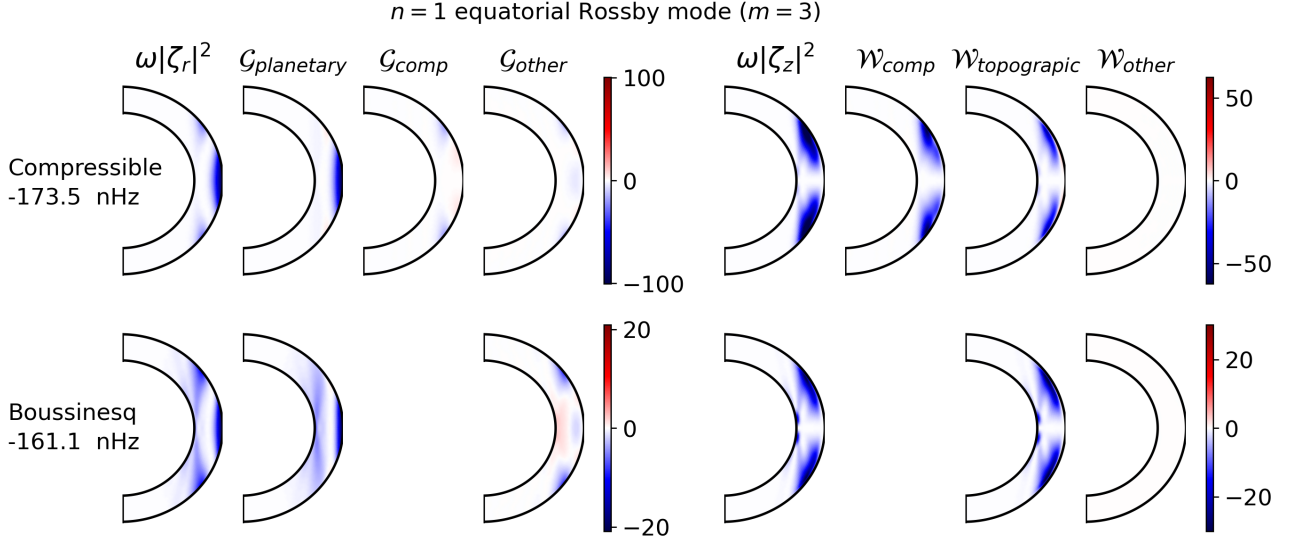


Fig. B.3. Relative importance of planetary β -effect ($\Re[\mathcal{G}_{\text{planetary}}]$), compressional β -effect ($\Re[\mathcal{G}_{\text{comp}}]$, $\Re[\mathcal{W}_{\text{comp}}]$), topographical β -effect ($\Re[\mathcal{W}_{\text{topographic}}]$) and other terms in the vorticity equation to determine the propagation and frequency of the $n = 1$ equatorial Rossby mode ($m = 3$) in the compressible and the Boussinesq models, under uniform rotation. The different quantities have the same definition and interpretation as in Fig. B.1. The respective frequencies of the modes are specified on the left. The eigenfunctions have the same normalization as in Fig. B.1.

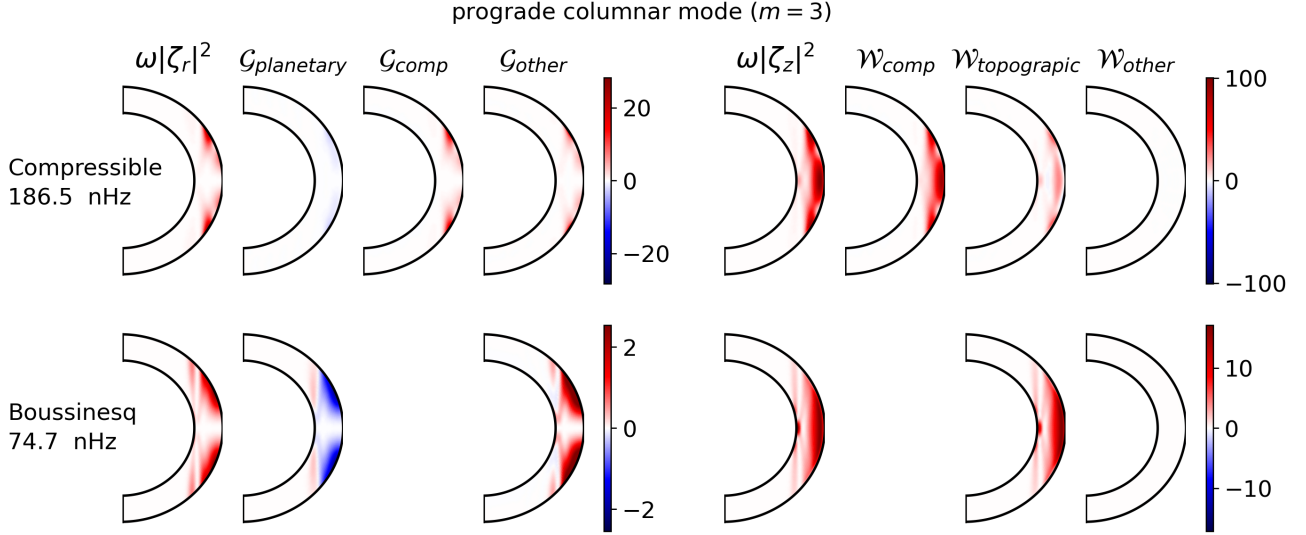


Fig. B.4. Relative importance of planetary β -effect ($\Re[\mathcal{G}_{\text{planetary}}]$), compressional β -effect ($\Re[\mathcal{G}_{\text{comp}}]$, $\Re[\mathcal{W}_{\text{comp}}]$), topographical β -effect ($\Re[\mathcal{W}_{\text{topographic}}]$) and other terms in the vorticity equation to determine the propagation and frequency of the prograde columnar mode ($m = 3$) in the compressible and the Boussinesq models, under uniform rotation. The different quantities have the same definition and interpretation as in Fig. B.1. The respective frequencies of the modes are specified on the left. The eigenfunctions from the different models are normalized to have the same integrated kinetic energy density such that the maximum of $\Re[\omega|\zeta_z|^2]$ is 100 for the compressible model.

under solar differential rotation and its corresponding entropy gradient. The non-toroidicity, represented as Γ , is calculated using the eigenfunction for the compressible model using Eq. (22). The tables show that the compressible and anelastic models have the same frequencies correct to 0.1 nHz. In contrast, the Boussinesq model has significantly different frequencies for almost all the modes except the $n = 0$ equatorial Rossby modes under uniform rotation. We find that the computation of the modes by the compressible model takes about 1.33 times the time taken for the modes computed by the anelastic model. Thus, the anelastic model simplifies the calculations without significantly affecting the solar inertial modes.

We plot the non-toroidicity of the modes computed using the compressible model against the absolute difference in the frequencies of the Boussinesq and compressible models under uniform and solar differential rotation in Fig. C.1. The frequency difference has an increasing trend with the non-toroidicity of the different inertial modes, in general. The trend is most prominently visible for the prograde columnar modes under both uniform and differential rotation and the high-latitude modes under differential rotation. It is also noticeable for the $n = 1$ equatorial Rossby modes under uniform rotation. However, the frequency difference decreases with the increase in azimuthal order for these modes (see Fig. 3). Under differential rotation, the non-toroidal effects of critical latitudes increase with the azimuthal

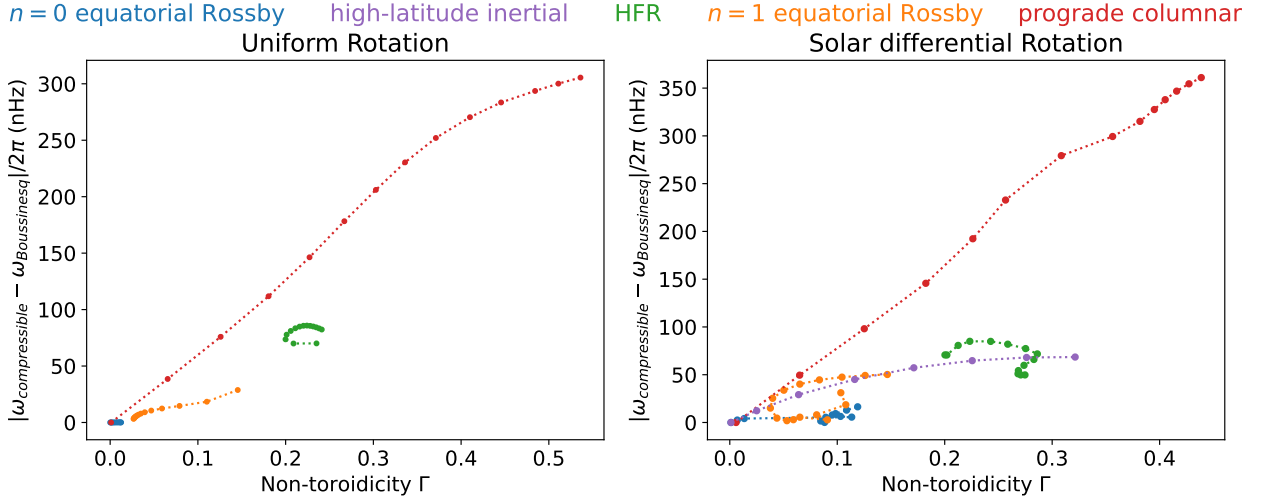


Fig. C.1. Effect of the non-toroidicity of the eigenmodes on the absolute difference of the real part of the eigenfrequencies between compressible and Boussinesq models. The non-toroidicity Γ of the eigenmodes is calculated using Eq. (22) for the compressible model. The right column corresponds to uniform rotation, and the left corresponds to solar differential rotation. The different colours denote the different modes like in Fig. 5. The different points of the same colour are for the modes with different azimuthal orders m .

Table C.1. Frequencies and non-toroidicity of the $n = 0$ equatorial Rossby modes under uniform rotation.

m	Compressible $\omega/2\pi$ (nHz)	Compr. - Anelastic	Compr. - Boussinesq	Γ
1	-455.9944	0.0056	0.0056	0.0000
2	-303.9977	0.0018	0.0020	0.0009
3	-227.9918	0.0008	0.0023	0.0019
4	-182.3657	0.0004	0.0061	0.0031
5	-151.9042	0.0002	0.0175	0.0045
6	-130.0859	0.0001	0.0388	0.0060
7	-113.6626	0.0001	0.0661	0.0076
8	-100.8461	0.0001	0.0907	0.0090
9	-90.5729	0.0001	0.1043	0.0103
10	-82.1683	0.0000	0.1026	0.0113
11	-75.1793	0.0000	0.0855	0.0120
12	-69.2873	0.0000	0.0562	0.0125
13	-64.2603	0.0000	0.0198	0.0127
14	-59.9249	0.0000	-0.0192	0.0128
15	-56.1494	0.0000	-0.0569	0.0127
16	-52.8323	0.0000	-0.0911	0.0125

Table C.2. Frequencies and non-toroidicity of the HFR modes under uniform rotation, with the same notation as in Table C.1.

m	Compressible $\omega/2\pi$ (nHz)	Compr. - Anelastic	Compr. - Boussinesq	Γ
2	-362.0800	0.0009	70.0505	0.2352
3	-329.3193	0.0007	69.9538	0.2090
4	-298.4230	0.0005	73.6560	0.1999
5	-270.5835	0.0004	77.7805	0.2011
6	-246.0950	0.0003	81.0767	0.2058
7	-224.7627	0.0002	83.4430	0.2110
8	-206.2202	0.0002	84.9281	0.2159
9	-190.0747	0.0002	85.6682	0.2203
10	-175.9641	0.0001	85.8339	0.2242
11	-163.5766	0.0001	85.5806	0.2279
12	-152.6507	0.0001	85.0296	0.2315
13	-142.9701	0.0001	84.2688	0.2349
14	-134.3562	0.0001	83.3587	0.2381
15	-126.6609	0.0001	82.3406	0.2412
16	-119.7606	0.0000	81.2419	0.2440

Notes. The first column denotes the azimuthal order m . The second column reports the frequency (ω) of the modes in the Carrington frame computed using the compressible model. The third and fourth columns report the differences in the frequencies (in nHz) for the anelastic and the Boussinesq models, respectively, from the compressible model. The fifth column denotes the non-toroidicity Γ computed for the modes from the compressible model using Eq. (22).

Table C.3. Frequencies and non-toroidicity of the $n = 1$ equatorial Rossby modes under uniform rotation, with the same notation as in Table C.1.

m	Compressible $\omega/2\pi$ (nHz)	Compr. - Anelastic	Compr. - Boussinesq	Γ
0	-274.9041	0.0011	-28.7642	0.1454
1	-238.8316	0.0008	-18.4009	0.1102
2	-203.4461	0.0005	-14.6810	0.0791
3	-173.4967	0.0003	-12.3822	0.0591
4	-149.3700	0.0002	-10.5521	0.0468
5	-130.1043	0.0001	-9.0625	0.0394
6	-114.6432	0.0001	-7.8716	0.0350
7	-102.1167	0.0001	-6.9313	0.0323
8	-91.8530	0.0001	-6.1867	0.0307
9	-83.3416	0.0000	-5.5842	0.0296
10	-76.1963	0.0000	-5.0785	0.0288
11	-70.1272	0.0000	-4.6374	0.0282
12	-64.9176	0.0000	-4.2419	0.0277
13	-60.4051	0.0000	-3.8832	0.0273
14	-56.4665	0.0000	-3.5580	0.0270
15	-53.0063	0.0000	-3.2646	0.0267
16	-49.9489	0.0000	-3.0020	0.0263

order. The competing effects complicate the non-toroidicity and frequency difference variation for the $n = 1$ equatorial Rossby modes under differential rotation. The variation of the frequency difference and the non-toroidicity is relatively small for the HFR modes under uniform rotation. Critical latitudes under differential rotation cause variations in the HFR modes. The $n = 0$ equatorial Rossby modes are almost entirely toroidal and have no frequency difference under uniform rotation. Under differential rotation, they have a slight non-toroidal character and frequency differences due to the radial motions near the critical latitudes for higher values of m . We note that non-toroidicity is not a very good measure for the differences, as more physics is involved

Table C.4. Frequencies and non-toroidicity of the prograde columnar modes under uniform rotation, with the same notation as in Table C.1.

m	Compressible $\omega/2\pi$ (nHz)	Compr. - Anelastic	Compr. - Boussinesq	Γ
0	0.0000	-0.0000	0.0000	0.0011
1	67.7673	-0.0004	38.5542	0.0656
2	130.7501	-0.0006	75.8710	0.1259
3	186.5260	-0.0008	111.8153	0.1806
4	235.2843	-0.0009	146.3101	0.2272
5	276.9278	-0.0009	178.2647	0.2669
6	310.8563	-0.0009	206.0269	0.3029
7	338.7767	-0.0009	230.3947	0.3361
8	362.0612	-0.0009	252.0103	0.3712
9	380.8134	-0.0008	270.4158	0.4101
10	393.3064	-0.0008	283.4660	0.4456
11	402.3409	-0.0007	293.6587	0.4843
12	407.2806	-0.0006	300.1433	0.5109
13	410.8534	-0.0006	305.4989	0.5360
14	412.0980	-0.0005	308.6629	0.5557
15	412.1763	-0.0005	310.7292	0.5672
16	411.6828	-0.0005	312.2481	0.5744

Table C.5. Frequencies and non-toroidicity of the $n = 0$ equatorial Rossby modes under solar differential rotation, with the same notation as in Table C.1.

m	Compressible $\omega/2\pi$ (nHz)	Compr. - Anelastic	Compr. - Boussinesq	Γ
1	-455.9953	0.0044	0.0047	0.0011
2	-331.8168	-0.0020	-2.5239	0.0070
3	-262.0695	-0.0134	-4.1339	0.0135
4	-230.0002	0.0083	-5.6185	0.1134
5	-197.0644	0.0017	-6.3740	0.1030
6	-171.2207	0.0024	7.8208	0.0954
7	-130.8246	-0.0040	0.0611	0.0882
8	-122.1143	-0.0014	1.5886	0.0847
9	-114.7690	-0.0016	5.4175	0.0893
10	-109.5107	-0.0021	9.2889	0.0984
11	-105.7246	-0.0025	12.9504	0.1087
12	-102.9795	-0.0028	16.4166	0.1190
13	-100.9864	-0.0031	19.6566	0.1291
14	-99.5498	-0.0032	...	0.1384
15	-98.5366	-0.0034	...	0.1459
16	-97.8500	-0.0035	...	0.1510

Table C.6. Frequencies and non-toroidicity of the high-latitude modes under solar differential rotation, with the same notation as in Table C.1.

m	Compressible $\omega/2\pi$ (nHz)	Compr. - Anelastic	Compr. - Boussinesq	Γ
0	-0.0000	-0.0000	-0.0000	0.0011
1	-95.6996	0.0034	12.2996	0.0250
2	-184.3896	0.0058	29.1408	0.0641
3	-270.5509	0.0200	45.0518	0.1163
4	-354.2757	0.0074	57.2498	0.1713
5	-434.7199	0.0068	64.7203	0.2256
6	-511.4853	0.0050	68.0383	0.2762
7	-584.4776	0.0029	68.4952	0.3214
8	-653.8597	0.0007	67.0029	0.3609

in the inertial modes. However, it gives a rough estimate of the differences in the eigenmodes caused by the Boussinesq approximation.

Table C.7. Frequencies and non-toroidicity of the HFR modes under solar differential rotation, with the same notation as in Table C.1.

m	Compressible $\omega/2\pi$ (nHz)	Compr. - Anelastic	Compr. - Boussinesq	Γ
2	-380.0809	0.0018	70.7218	0.2002
3	-350.1367	0.0027	70.6547	0.2020
4	-320.1066	0.0039	80.6738	0.2125
5	-293.3019	0.0053	84.9598	0.2234
6	-270.2756	0.0068	84.8862	0.2428
7	-251.0942	0.0083	81.9565	0.2587
8	-235.3597	0.0096	77.3598	0.2753
9	-222.3900	0.0104	71.7780	0.2862
10	-211.2815	0.0097	65.9498	0.2830
11	-202.2048	0.0075	59.8404	0.2738
12	-195.3937	0.0055	54.3140	0.2686
13	-190.3007	0.0042	50.9713	0.2682
14	-186.2602	0.0035	49.7995	0.2708
15	-182.8271	0.0030	49.7990	0.2747
16	-179.7445	0.0025	50.2232	0.2790

Table C.8. Frequencies and non-toroidicity of the $n = 1$ equatorial Rossby modes under solar differential rotation, with the same notation as in Table C.1.

m	Compressible $\omega/2\pi$ (nHz)	Compr. - Anelastic	Compr. - Boussinesq	Γ
0	-288.5330	0.0004	-31.1401	0.1033
1	-246.9782	0.0007	-18.5591	0.1079
2	-210.5457	0.0007	-8.0265	0.0808
3	-182.0516	-0.0001	2.7757	0.0908
4	-151.9285	-0.0003	5.5443	0.0652
5	-129.2566	-0.0007	2.9265	0.0592
6	-108.2980	-0.0023	-1.8894	0.0531
7	-89.0665	-0.0047	4.5684	0.0439
8	-73.4214	-0.0080	15.0778	0.0378
9	-60.4377	-0.0117	25.3317	0.0399
10	-49.7833	-0.0136	33.7863	0.0503
11	-41.1950	-0.0128	40.1575	0.0652
12	-34.2704	-0.0104	44.6014	0.0834
13	-28.4929	-0.0083	47.4666	0.1044
14	-23.3225	-0.0071	49.2240	0.1260
15	-18.4022	-0.0064	50.2401	0.1466
16	-13.5597	-0.0059	50.7363	0.1661

Table C.9. Frequencies and non-toroidicity of the prograde columnar modes under solar differential rotation, with the same notation as in Table C.1.

m	Compressible $\omega/2\pi$ (nHz)	Compr. - Anelastic	Compr. - Boussinesq	Γ
0	-0.0000	-0.0000	-0.0000	0.0058
1	76.7750	0.0002	49.5405	0.0650
2	147.6312	0.0004	98.1219	0.1252
3	210.8393	0.0009	145.6926	0.1824
4	267.4129	0.0017	192.3226	0.2262
5	316.0582	0.0025	232.8312	0.2566
6	370.4610	0.0029	279.3092	0.3085
7	400.2431	0.0029	299.3421	0.3563
8	423.8501	0.0033	315.1826	0.3817
9	443.9587	0.0034	327.5663	0.3951
10	461.9409	0.0033	337.8791	0.4052
11	478.4130	0.0031	346.8144	0.4158
12	493.5135	0.0028	354.5033	0.4273
13	507.3183	0.0026	361.0170	0.4387
14	519.9892	0.0025	...	0.4496
15	531.7273	0.0024	...	0.4598
16	542.7219	0.0024	...	0.4692